Physics of Fluids

The vortex ring state of a rotor and its comparison with the collapse of an annular jet in counterflow

Cite as: Phys. Fluids **35**, 044103 (2023); https://doi.org/10.1063/5.0143406
Submitted: 23 January 2023 • Accepted: 16 March 2023 • Accepted Manuscript Online: 17 March 2023 • Published Online: 04 April 2023

Published open access through an agreement with JISC Collections

D. J. Pickles, R. B. Green and A. Busse

View Online Export Citation CrossMark

ARTICLES YOU MAY BE INTERESTED IN

A mixing enhancement mechanism for a hydrogen transverse jet coupled with a shear layer for gas turbine combustion
Physics of Fluids **35**, 045111 (2023); https://doi.org/10.1063/5.0142960

A systematic investigation on flow characteristics of needle-ring-net electrohydrodynamic gas pump
Physics of Fluids **35**, 047108 (2023); https://doi.org/10.1063/5.0140445

Optimization study on adaptive control performance of shock wave/boundary layer interactions with different secondary recirculation configurations
Physics of Fluids **35**, 045114 (2023); https://doi.org/10.1063/5.0142076

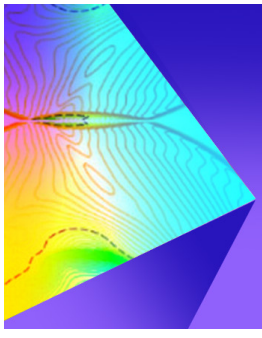

Physics of Fluids
Special Topic: Shock Waves
Submit Today!

AIP Publishing

© 2023 Author(s).

Physics of Fluids ARTICLE scitation.org/journal/phf

The vortex ring state of a rotor and its comparison with the collapse of an annular jet in counterflow

Cite as: Phys. Fluids **35**, 044103 (2023); doi: 10.1063/5.0143406
Submitted: 23 January 2023 · Accepted: 16 March 2023 ·
Published Online: 4 April 2023

View Online Export Citation CrossMark

D. J. Pickles, R. B. Green,[a] and A. Busse

AFFILIATIONS

Aerospace Sciences, James Watt School of Engineering, University of Glasgow, Glasgow G12 8QQ, Scotland, United Kingdom

[a]Author to whom correspondence should be addressed: richard.green@glasgow.ac.uk

ABSTRACT

The vortex ring state (VRS) of a rotor is associated with the development of the trailed vortex system in powered descending flight, where the topology of the vortex wake changes from its usual helical form into a toroidal form. In the VRS, the toroidal vortex ring envelops the entire rotor, and it sheds and reforms in an unsteady manner. In previous attempts to understand the basic phenomenology of the VRS, the focus was on the role of the trailed vortices in the transition to the VRS: computational and experimental work utilized rotor models to generate the trailing vortex wake, and mechanisms for the emergence of the VRS were postulated based on the interaction of the trailed vortices. In this paper, a different approach is taken: a set of experiments on a core annular jet flow are described, where the jet flow in counterflow is used to simulate a rotor in powered descent. It is shown that this leads to the formation of a flow field that shares many of the features of the VRS of a rotor system. This brings into question the role of the rotor blade trailing vortices in the development of the rotor wake VRS, and it is proposed instead that the interaction between the mean flow and counterflow drives the VRS phenomenon.

© 2023 Author(s). All article content, except where otherwise noted, is licensed under a Creative Commons Attribution (CC BY) license (http://creativecommons.org/licenses/by/4.0/). https://doi.org/10.1063/5.0143406

I. INTRODUCTION

Flows associated with the aerodynamics of rotorcraft exhibit a wide range of fascinating phenomena, including vortex dominated flow, regions of high compressibility, unsteady flow, attached and separated flows, and interaction phenomena. Compared to fixed-wing flight, the rotor-trailed vortices remain in the vicinity of the lifting surfaces and airframe for a long time. This on its own is responsible for many of the challenges unique to rotorcraft design and performance. Typically, the rotor blades trail a set of inter-twined vortices; in a hover, they form a helical trailed vortex wake below the rotor; in forward flight, this wake is skewed backward. Many descriptions of the rotor wake in the hover are available in the literature, see Martin, Bhagwat, and Leishman[1] for example.

The vortex ring state (VRS) of a rotor occurs under particular conditions of powered descending flight. A characteristic scaling velocity for a rotor flow is the hover-induced velocity V_h, the mean flow velocity through the rotor disk induced by the rotor in the hover that is dependent upon the rotor thrust. In powered descending flight at descent rate V_d, the rotor is descending in the direction of its own wake flow, and at sufficiently high descent velocity ratios $V_d \approx V_h$, the rotor descends into its own wake. The rotor wake then forms a large, toroidal vortex structure, that breaks away and reforms, this is the vortex ring state. A schematic diagram of a rotor wake in the VRS is indicated in Fig. 1; important topological features are the vortex ring that contains the trailed vortices that are normally below the rotor disk, the saddle point below the rotor and the reverse flow penetrating up toward the disk. VRS phenomena have been observed since the early days of propeller powered flight,[2] and issues associated with the descent of a rotor toward its own wake have been reported since the early days of rotary winged flight. From a performance perspective, large thrust oscillations, an increase in average power required, and loss of control efficiency characterize the entry into the VRS regime, which can lead to loss of the aircraft,[3,4] with in-flight tests[5] and experiments[6] in the 1950s providing some insight. The VRS was identified as a flight regime to avoid, and piloting strategies evolved, but United States and United Kingdom authorities ascribed the loss of 32 helicopters to VRS between 1982 and 1997.[7] The development of the Bell-Boeing V22 Osprey tilt-rotor in the United States was compromised by a mishap associated with the VRS,[8] so any novel rotor configuration should be developed with the consequences of VRS behavior in mind. Multi-rotor drones and future concepts for air travel using distributed rotor systems need to have VRS mitigation strategies in their systems design, and the VRS is a flow regime known to be of importance for floating wind turbines.[9,10] A rotor VRS is therefore an

© Author(s) 2023

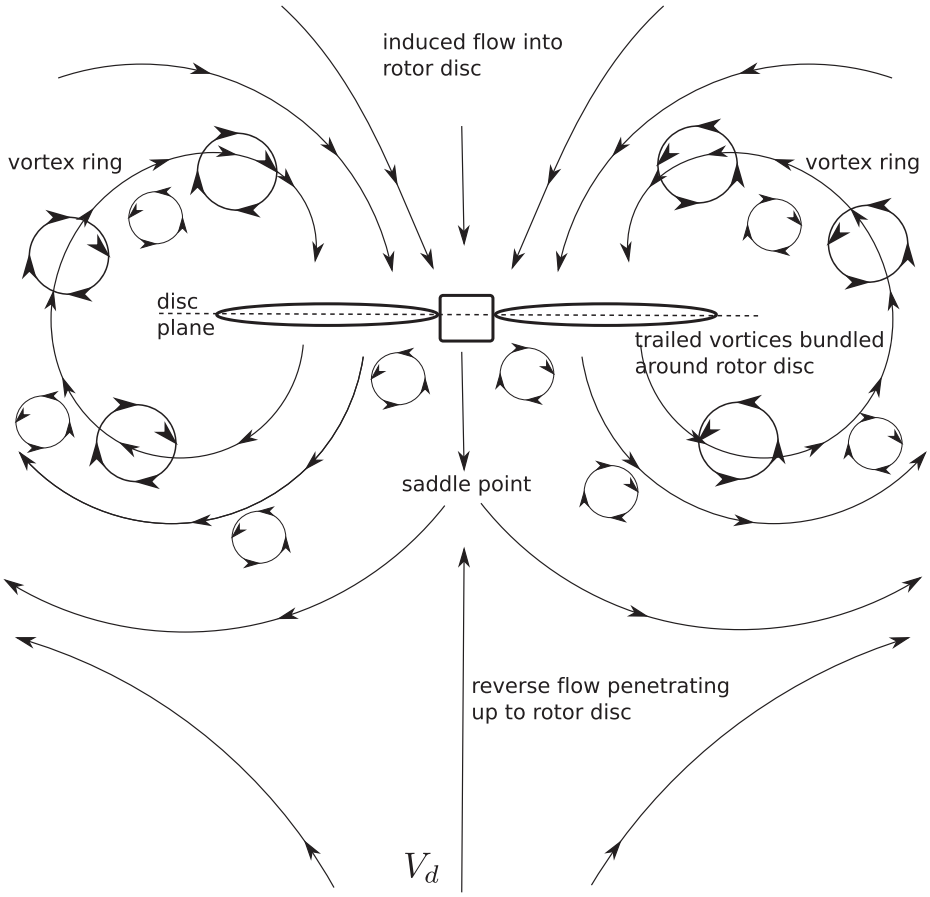

FIG. 1. Schematic diagram of a rotor wake in VRS, observer moving with the rotor descending into quiescent air at descent rate V_d.

important phenomenon to investigate from the perspective of its interesting fluid dynamics and practical significance for rotor systems. This paper presents an outline description and review of the phenomenon and then considers an experimental analog of the VRS of a rotor in the form of an investigation of a specific annular jet configuration in a counterflow.

Aspects of rotor performance in VRS were the primary motivating factors for the study. Initial investigations of rotor performance performed by Gessow,[11] Lock *et al.*,[12] Glauert,[13] and Castles and Gray[14] attempted to calculate performance parameters such as rotor inflow, induced velocity, thrust, and power through actuator disk theory and simple stream tube models. More recent research using this kind of theory includes the work of Newman *et al.*,[15] Spalart,[16] and Taghizad *et al.*[17] These approaches help to define the VRS onset boundary, and Spalart[16] comments on the VRS being in between the two streamtube flow types for climb (including hover), and rapid descent, for which the flow through the disk is in distinctly different directions. Such low-order models are valuable, but their ability to capture the complex flow physics of the VRS is limited. Flight testing to evaluate VRS has been reported by Reeder and Gustafson,[3] Brotherhood,[4] Stewart,[5] Gessow,[11] and Taghizad *et al.*[17] among others. Experimental research on model rotors has followed a number of strands. Disk loading and blade twist were investigated experimentally by Castles and Gray,[14] Yaggy and Mort,[18] Washizu *et al.*,[19] Azuma and Obata,[20] and Newman *et al.*[21] Here, the thrust and torque produced by a variety of different rotors were measured as the descent velocity of the rotors was varied, trends resulting from the blade twist were observed in some of these experiments. Within other work, including the study of Brinson,[22] a non-dimensional descent rate range has been identified in which momentum theory is not valid, and the VRS occupies only a part of this range. Recent attention has turned to the VRS of multiple rotor systems,[23] where broadly similar phenomena were observed, but the rotor spacing was found to affect the flow structure of the inner part of the rotor wake due to rotor–rotor interaction.

Characterization of the fluid dynamics of the VRS commenced with the smoke flow visualizations performed by Drees and Hendal,[6] which show the entire rotor contained in the vortex ring. A characteristic of the VRS is a conical region of reverse flow can penetrate up through the center of the rotor.[22] This has been observed both in flow visualization and anemometry. Under some experimental descent conditions, Stack *et al.*[24] and Savaş *et al.*[25] showed experimentally that the periodic detachment of the vortex ring from the rotor disk plane is associated with periodic oscillations of the rotor thrust. Quantitative particle image velocimetry (PIV) measurements of the flow field produced by a model rotor operating in axial descent were performed by

© Author(s) 2023

Green *et al.*[26] At low descent velocities, the mean flow field below the rotor resembled that of a rotor operating in the hover, whereas at high descent rate, a region of reverse flow toward the rotor was observed. At intermediate descent rates, the flow switched between those two states. The conical region of reverse flow reported by Brinson[22] was observed in these measurements also. The work presented by Leishman *et al.*[27] considered the bundling of vortex filaments around the edge of the rotor disk in the transition to the VRS; instabilities caused perturbations to reach sufficiently high amplitudes such that the breakdown of the helicoidal wake was the consequence.

Investigation of the VRS using computational fluid dynamics (CFD) requires methods that can preserve the rotor blade trailing vortices for the long non-dimensional times. Free-wake simulations of a helicopter rotor in axial descent performed by Leishman *et al.*,[27] Bhagwat and Leishman,[28] and Ananthan and Leishman[29] associated a mutual-inductance instability, sometimes known as the "vortex pairing" mode, with the bundling of vortex filaments into rings, which move toward the rotor as it approached the VRS. High resolution CFD simulations of a rotor entering the VRS from the windmill brake state and from the hover using a Vorticity Transport Model (VTM) were presented by Brown,[30] and results are reported elsewhere by Ahlin and Brown[31] among others. When the rotor transitioned into the VRS from the windmill brake state, the blade tip vortices reorientated themselves to form a hairpin structure, which was then ejected from the wake. This ejection vortex disrupted the formation of the normal helical vortex structure for several rotor revolutions. Hairpin vortices were not observed in the rotor wake when it transitioned from hover into the VRS, indicating that the underlying mechanism may differ depending on the way the rotor enters the VRS. These simulations also showed that the up flow through the rotor root section, identified by Brinson[22] and Green *et al.*,[26] was dependent on the blade root-vortex system, and the dynamics of this element of the wake structure should not be ignored.

Various computational and experimental approaches to investigation of the VRS have used rotor models as their physical basis. This is understandable, and, consequently, descriptions of the phenomena have tended to concentrate upon the fate of the blade trailing vortices. As described in this introduction, however, simple stream tube models (with actuator disk theory) of the rotor wake on either side of the VRS have been very powerful, see Spalart.[16] The stream tube in its simplest form has a top hat jet velocity profile. Behavior of a conventional top-hat jet in a uniform counterflow is a classical problem in fluid mechanics, and work with round jets in counterflow has been the subject of some interest. At low counter flow (U_o) to jet velocity (U_i) ratios $(\alpha = (|U_o|/U_i)$, the flow field is divided into two regions: the near field where the flow field is similar to that of a jet issuing into quiescent surroundings; and the far field where the jet interacts with the counterflow. The interaction of the jet with the counterflow is associated with the movement of the jet tip, as described by König and Fiedler,[32] Hopkins and Robertson,[33] and Yoda and Fiedler.[34] At higher counterflow to jet velocity ratios, the round jet forms an axisymmetric vortex ring around the nozzle exit which is periodically shed. This behavior is somewhat similar to aspects of elements of the VRS of a rotor. A jet flow may be characterized in terms of its mean flow velocity profile; it is, thus, informative to consider the structure of the mean flow of a rotor wake in hover in comparison. While the rotor trails a helical vortex structure, the mean flow field reveals a flow structure akin to an axisymmetric, core-annular jet consisting of a ring of high momentum flow close to the edge of the rotor disk, with relatively low momentum flow around the rotor axis. This poses the question: How does a jet with this structure behave in a counter-flow? Does the structure of the corresponding flow resemble that of a rotor in axial descent?

With the above discussion in mind and to gain further insight into the rotor wake VRS, experiments on a axisymmetric, core-annular jet in counterflow have been conducted and are reported in this paper, and a comparison with the VRS of a rotor in axial descent is made. A device to create a jet flow with similar characteristics to the time-mean flow of the velocity profile of a rotor wake in hover was tested in a wind tunnel, with the wind tunnel free stream in counterflow to the jet acting as an experimental model of descent. The flow field development was investigated using flow visualization, Laser Doppler Anemometry (LDA) and Particle Image Velocimetry (PIV). A rotor system was tested for purposes of comparison, and the jet in counterflow is observed to break down into a VRS in a manner similar to a rotor in axial descent.

II. EXPERIMENTAL METHOD

This section describes the design of the jet system, the wind tunnel, and its instrumentation and includes a description of a rotor system used for comparison.

A. Ventilated open core annular jet

To create a jet in counterflow, a bespoke nozzle system was placed in a wind tunnel where the jet flow produced by the nozzle was subject to a range of counterflow velocities ranging from $\alpha = \frac{U_o}{U_i} = 0$ to 1.8, where U_i is the mean velocity of the jet to give the same momentum across the exit plane of the jet body (equivalent to rotor hover induced velocity V_h, which is the mean velocity induced at the disk to produce the same thrust in hover), and U_o is the free stream velocity in the wind tunnel, the counterflow velocity, equivalent to rotor descent rate V_d. The jet system should create a stream tube that contains the jet mechanism as if it were a rotor; it should have an inflow to the jet mechanism, and then produce the same mean flow characteristics as a rotor wake in hover. A suitable design is based upon a commercially available so-called bladeless fan or air multiplier.[35] In the literature these sorts of appliances are referred to as ventilated open core annular jets (OCAJ).[36–38] Figure 2 shows the general concept. Air is pumped into a ring with a hollow interior that acts as a plenum chamber. The cross section of the ring body resembles a thick airfoil, and the radially inward facing surface of the ring forms the nozzle surface contour. Air flows out of a continuous azimuthal slot cut into the nozzle inward facing surface to form an annular jet. This jet remains attached to the inward facing nozzle surface contour by the Coandă effect[39] and the jet flow entrains air through the center of the ring in the ring axial direction. The jet geometry will be referred to as a ventilated open-core annular jet (OCAJ).

The annular nozzle used in the present experiments, shown in Fig. 3, was designed with the aid of CFD to create as uniform a flow around the azimuth as possible, and was 3D printed out of Accura Xtreme White using SLA, which gave a smooth surface finish. The design consists of a plenum and a uniform exit slot located around the inward facing curved surface of the nozzle. The slot outer and inner diameter dimensions D_o and D_i are provided in Table I. The slot width varied by $\pm 0.5\%$ around the azimuth of the nozzle. An air

© Author(s) 2023

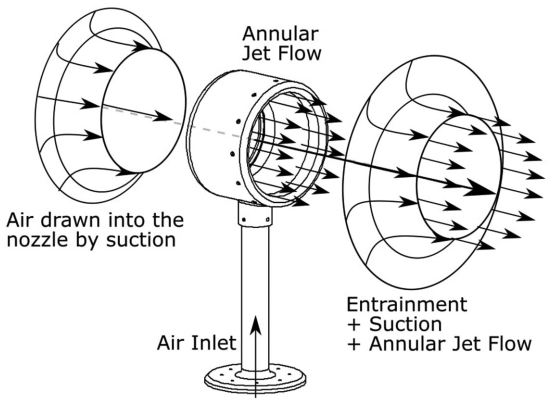

FIG. 2. Bladeless fan or air multiplier concept forming the basis of the open core annular jet.

compressor provided a continuous supply of air through a long pipe into the plenum at a rate of $Q_0 = 0.01 \pm 0.001\ \mathrm{m^3\ s^{-1}}$ with a back pressure of 7.7 bar, the air flow leaving the OCAJ plenum through the slot outlet. The flow rate was monitored using a Dwyer Instruments VFC-123 flow meter for the duration of each experiment, and the temperature of the jet was equal to the ambient air flow. The radius of the OCAJ at the exit plane of the assembly is $R = 0.079$ m. An (x, y, z)-coordinate system with its origin at the geometric center of the nozzle outlet plane is shown in Fig. 3 and defined such that the y-axis is vertically upward and the x-axis is in the direction of the OCAJ induced flow.

B. Rotor system for comparison

An experimental investigation into the flow field produced by a $R = 0.0895$ m radius, two bladed, twisted, tapered, fixed pitch rotor was also performed. For comparison with the OCAJ, additional tests with this rotor mounted in a shroud were conducted. The rotor and shroud are shown in Fig. 4. The rotor had no cyclic input and there were no lead-lag or flap degrees of freedom. Figure 5 shows the chord c, thickness t, and blade pitch distribution of the blade. The fiberglass rotor was lightly loaded and assumed to be rigid. The rotor was powered by a brushless motor, which was mounted on a stand located inside the wind tunnel. Figure 4 shows the rotor mounted in the shroud body. The shroud was connected to the motor using three support struts located on the inlet side. For all tests, the rotor was operated at a constant rotational frequency of 66.3 ± 1 Hz, producing a rotor tip speed of $V_{\mathrm{tip}} = 37\ \mathrm{m/s^{-1}}$ and a blade tip Reynolds number of 15 000. The motor and propeller chosen were readily available components for small drones. The shroud, shown in Fig. 4, was 3D printed out of prototyping polylactic acid (PLA) The internal contour shape was designed based on the investigation performed by Pereira[40] to optimize the hovering performance of a shrouded rotor. The rotor disk plane was located at the throat of the shroud, and the shroud had an inlet lip radius of $r_{\mathrm{lip}} = 0.22R$, a blade tip clearance $(\delta_{\mathrm{tip}} \approx 0.001\ \mathrm{m})$, a diffuser angle $\theta_d = 10°$, and a diffuser length of $L_d = R$. Rather than a single surface, inner wall-only shroud, which is characteristic of shrouds used to characterize the performance of hovering shrouded rotors, a smooth curve was used to define the external profile of the shroud, as seen in Fig. 4.

TABLE I. Table of OCAJ nozzle parameters: Outer and inner dimensions of the slot D_o and D_i. Jet outlet slot width l. Uniform exit velocity from the slot U_{ex} calculated from mass conservation. Radius R of OCAJ at the exit plane of the assembly. Jet outlet Reynolds number $R_{ej} = \frac{U_{ex} l}{\nu}$.

D_o (m)	D_i (m)	$\frac{D_i}{D_o}$	l (m)	U_{ex} $\mathrm{ms^{-1}}$	R (m)	R_{e_j}
0.0684	0.0667	0.98	0.0017	39.4	0.079	5253

C. Arrangement of experimental systems in the wind tunnel

The OCAJ nozzle and rotor assemblies were placed in the working section of the University of Glasgow deHavilland wind tunnel.

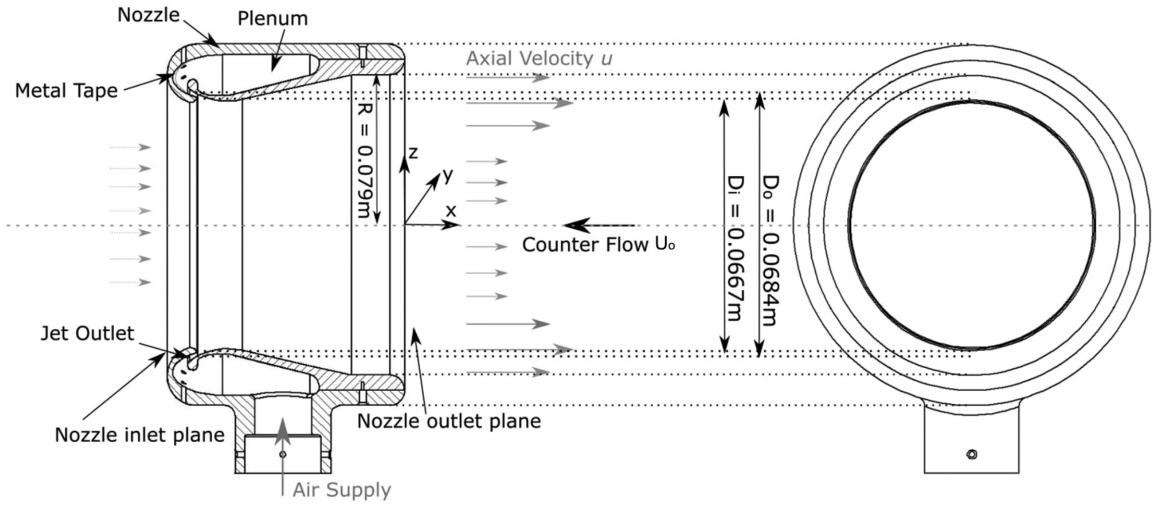

FIG. 3. Design of the open core annular jet. Coordinate system (x, y, z) has its origin at the center of the nozzle outlet plane indicated, (y, z) plane is in the exit plane.

© Author(s) 2023

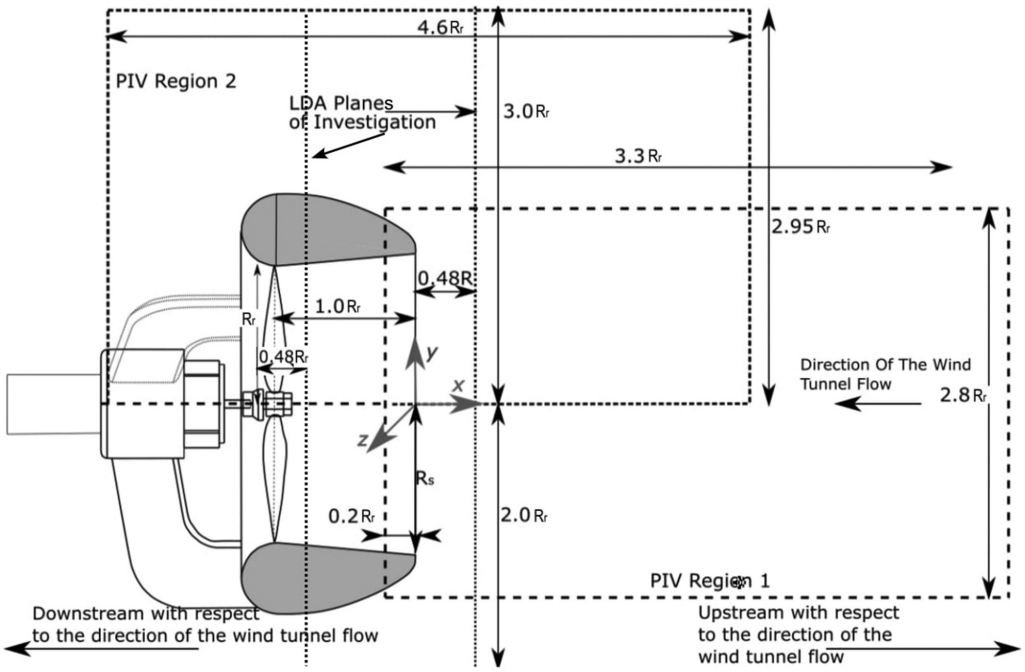

FIG. 4. Schematic diagram of the rotor system and shroud used for this investigation. Figure adapted from Ref. 41.

This is an atmospheric, closed-return, low-speed wind tunnel with a 2.66 m wide, 2.06 m high, and 5.4 m long octagonal test section, with a turbulence intensity below 0.2%. The OCAJ nozzle was placed with its axis in the counterflow direction to the wind tunnel free stream at a height of 1 m above the tunnel floor. The test rig has a wind tunnel blockage of 2.9%, and this investigation can be regarded as an investigation of an unconfined jet in counterflow. The terms upstream and downstream are used in the wind tunnel sense; thus, the OCAJ jet axial direction x is upstream. Homogeneous seeding of the wind tunnel for Particle Image Velocimetry (PIV) and Laser Doppler Anemometry (LDA) was achieved using a Pivtec-GmbH PIV Part 160 seeder, which produced a mean particle diameter of 0.9 μm using olive oil as the substrate.[42]

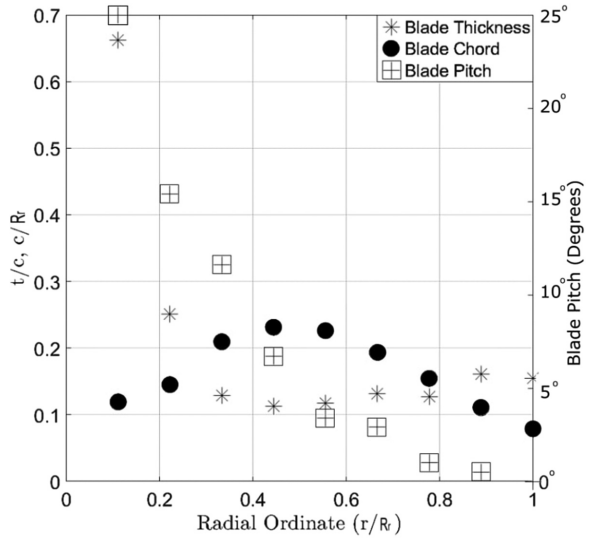

FIG. 5. Chord, thickness, and pitch profiles of the rotor blade used in this investigation.

D. Instrumentation

A commercially available Dantec Dynamics three-component Laser Doppler Anemometry (LDA) system was used to investigate the velocity profile 0.48R upstream of the nozzle outlet plane and 0.1R downstream of the nozzle inlet plane. The system operated on the dual beam, frequency shifted principle in backscatter. The system consists of three diode pumped solid state 1 W lasers at wavelengths of 488, 514, and 532 nm mounted on a Dantec 9041T3332 3D $1 \times 1 \times 1\ m^3$ traverse system capable of scanning the measurement volume with a positional accuracy of $\pm$ 0.01 mm. The 488 and 514 nm lasers were fed by optical fiber into a two-component probe oriented at angles of 2.5° from the horizontal and vertical axes, and the 532 nm laser was fed by optical fiber into a single-component probe oriented at 28° to the y axis. Each probe was fitted with a 2 m focal length beam expander, and the six beams coincided where the probe axes met to form a $2.62 \times 0.12 \times 0.12\ mm^3$ ellipsoidal measurement volume. Light scattered back to the probe heads was fed to the photodetectors by optical fiber and subsequently to the burst spectrum analyzers. In anticipation of elevated turbulence levels associated with jet counter flows and to avoid velocity-bias effects, the system was operated in the burst mode with transit (residence) time enabled for the calculation of

© Author(s) 2023

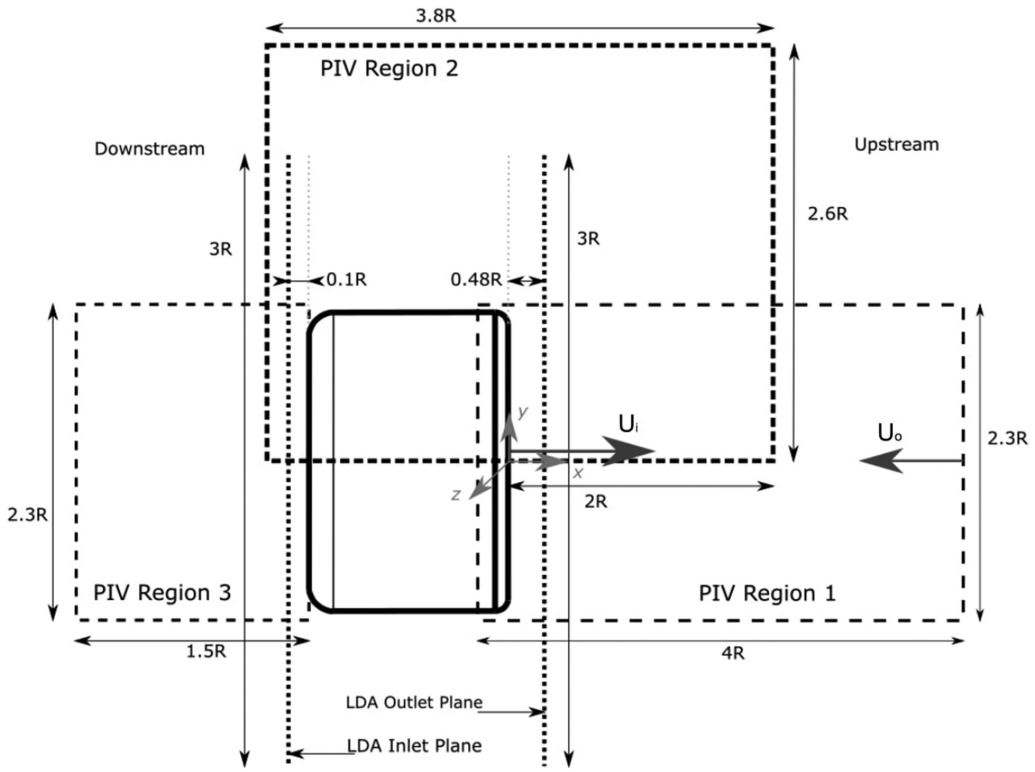

FIG. 6. Schematic diagram of the PIV regions of interest and the LDA planes investigated relative to the OCAJ nozzle body. The OCAJ induced velocity is from left to right, the wind tunnel counter flow is from right to left.

the mean flow velocity.[43,44] The LDA measurement volume was scanned across the inlet and exit planes to the OCAJ as indicated in Fig. 6.

Two-component PIV in the vertical symmetry plane along the longitudinal centerline of the jet was performed. A Litron LPY series, dual cavity, oscillator-amplified, frequency-doubled Nd:YAG laser with an output energy of 100mJ per pulse at 532 nm wavelength was used for illumination, with beam shaping optics and a cylindrical lens to deliver the light sheet. A Phantom v341 high speed, 4 megapixel camera with a 2560 × 1600 pixel CMOS sensor fitted with a 85 mm focal length lens set to f# = 1.8 was used to acquire the raw images. Calibration was performed by recording images of a 5 mm pitch dot pattern with the calibration grid aligned with the laser sheet plane. A quadratic, least squares fitting function was made to the dot pattern. The flow field was split into three distinct regions as shown in Fig. 6 to study the flow into, out of and around the nozzle. 600 image pairs were recorded at up to 200 Hz for a range of counterflow velocities; lower PIV data rates around 20 Hz were used when the slowly developing transient VRS phenomena were being captured. A time delay of $\Delta t = 100\mu s$ between each image in the pair was used for all experimental configurations.

Smoke flow visualization was used to investigate the structure of the flow field. A smoke filament was generated using a wand with a heated tip that vaporized mineral oil pumped onto it. The wand was placed at strategic locations in the wind tunnel (usually upstream of the OCAJ), so that the smoke was entrained into the flow phenomena of interest. Images were recorded at 300 frames per second for up to 30 ss using a high-speed camera.

E. LDA analysis methodology and accuracy

Characterization of the OCAJ nozzle inlet and outlet flows was performed on a grid of sample points in concentric circles centered around the nozzle axis with azimuthal and radial resolutions of 15° and 0.05R, respectively. For these characterization tests, each of the 441 data points was sampled over a period of 10 s with data burst rates maintained above 300 counts per second. The approximate accuracy of the mean flow velocity was calculated as 0.02 ms^{-1}, which corresponds to 0.22% of the peak nozzle outlet velocity. In counterflow, each of the 102 data points was sampled for 30 s along the vertical and horizontal axes of symmetry of the nozzle, with a spatial resolution of 0.04R, except for the cases where the counterflow velocity ratio was equal to $\alpha = 0.8$ and 0.9. For these test conditions, each data point was sampled for a duration of 90 s in order to obtain the time-averaged velocity with the same confidence. Only 2-component LDA (u, v) was achievable at the inlet of the OCAJ. The accuracy of the LDA system is dependent on the alignment of the laser system and the traverse with respect to the wind tunnel-free stream. The mount onto which the probes were attached allowed the angle of the probe to be measured with an accuracy of ± 0.5°, and the alignment of the traverse to the wind tunnel axis was measured to be less than 0.5° by

© Author(s) 2023

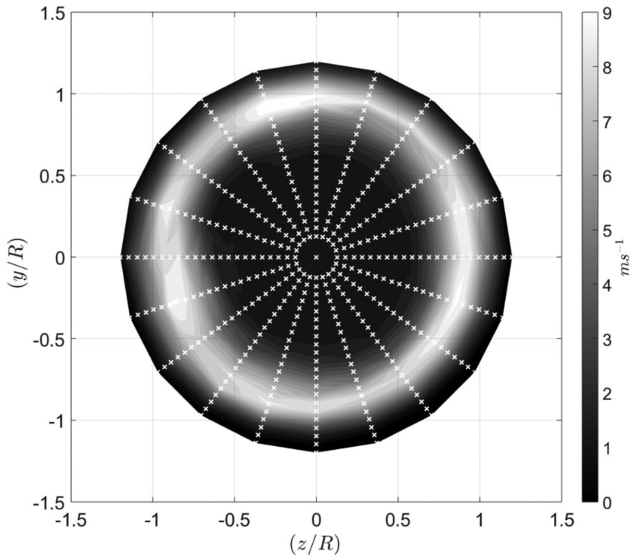

FIG. 7. Averaged axial (u-) velocity component (ms^{-1}) of the OCAJ nozzle outlet from LDA in zero counterflow 0.48R upstream of the nozzle outlet plane. Each sample point location is displayed by the white crosses.

measuring the movement of the laser focal point from the centerline of the wind tunnel over a 1 m traverse.

F. PIV analysis, methodology and accuracy

Post-processing of the raw PIV images was completed using a well established cross correlation-based procedure, using the same scheme described by Green *et al.*[26] PIV of image regions closer than 3 mm to the solid surfaces were unreliable as a result of glare. The results presented in this paper were produced with an interrogation sub-window size of 32 × 32 pixels with a 50% overlap. The resolution of the PIV was approximately 0.051R × 0.045 per vector for all regions of interest (without overlap). To mitigate against peak-locking, a continuous window shift technique was incorporated into the correlation-based interrogation algorithm. This has been shown by Gui and Wereley[45] to remove the effect that non-uniformly distributed bias errors have on the accuracy of the correlation-based tracking algorithm used to process PIV images. The uncertainty of the velocity measurements was estimated to be $\varepsilon_u = \frac{0.1}{M\Delta t} = \pm 0.05\,\mathrm{ms}^{-1}$ for the displacement measurement error of 0.1 pixels, where M is the magnification in pixels/mm. Post-processing of the data produced the mean velocity profile of the flow field.

III. RESULTS

A description of the flow field generated by the OCAJ issuing into quiescent surroundings is provided. This characterizes the mean velocity profile of the jet. A description of the effect of the counterflow on the OCAJ flow then follows. The emphasis is on the OCAJ behavior, but results of rotor wake behavior are described also. The scaling velocity notation used throughout this paper is U_i for the OCAJ and V_i for the rotor, and these are described in the relevant sections To follow.

A. Characterization of the OCAJ flow field

The OCAJ flow time-averaged axial velocity component u from LDA measurements in a cross-stream plane $0.48R$ away from the nozzle outlet plane is shown in Fig. 7 for zero counterflow. The induced velocity of the jet, $U_i = 4.5\,\mathrm{m/s}$ is the mean velocity of the jet based

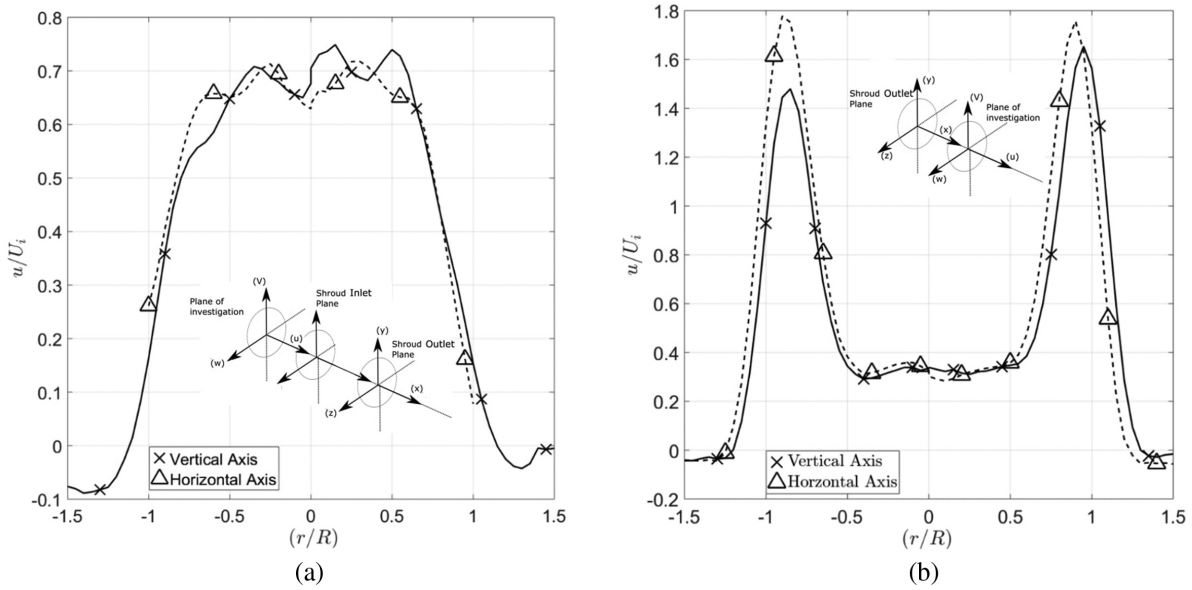

FIG. 8. Axial (u-) velocity profiles along the vertical and horizontal axis of symmetry of the nozzle from LDA survey of OCAJ in zero counterflow. Frame (a) inlet plane $\left(\frac{x}{R} = -1.75\right)$, frame (b) exit plane $\left(\frac{x}{R} = 0.48\right)$. Data are scaled with respect to the notional induced velocity U_i at the OCAJ exit. The vertical and horizontal axis directions refer to the direction of the LDA scan.

© Author(s) 2023

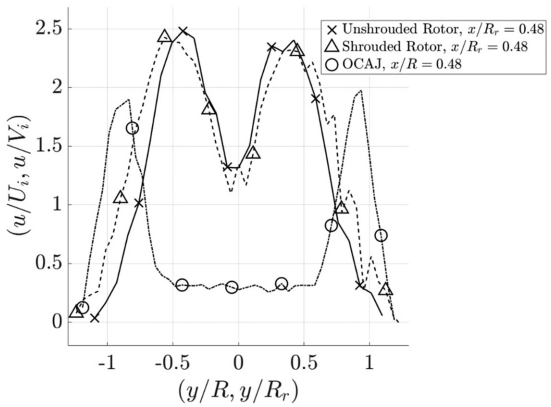

FIG. 9. Mean axial velocity profile produced by the OCAJ and both the shrouded and unshrouded rotors from LDA. U_i and R are the OCAJ scaling velocity and radius, V_i and R_r are the rotor scaling velocity and radius. With the axis systems defined the measurement planes were all at 0.48 radius.

upon the mass flow rate. Note that the hover induced velocity of a rotor V_h is based upon the rotor thrust, the jet thrust is not measured here. Previous investigations of jet flows in counterflows such as the study of Morgan, Brinkworth, and Evans[46] have used momentum flux to scale the counterflow with respect to the jet flow. This does not include the influence of the ventilated core on the velocity profile; however, therefore a notional induced velocity U_i based on mass flow was used instead. LDA velocity profiles along the vertical and horizontal axes of symmetry of both the nozzle inlet and outlet planes extracted from Fig. 7 are presented in Fig. 8. The inlet and exit planes show a small departure from axisymmetry; the maximum variation is 8% around the azimuth for the outlet mean axial flow. The inlet to the OCAJ shows weak negative u at the extreme values of radial ordinate r; this is beyond the inlet lip of the OCAJ and part of the induced flow behavior. High values of u are observed closer to the OCAJ axis, and the axial inlet velocity is almost uniform over a wide range of r. The jet exit plane shows a very different profile, as this contains the annular jet in addition to the induced core flow. The axial velocity profile of the OCAJ is represented as a region of relatively uniform axial flow around the nozzle axis surrounded by a ring of high velocity air associated with the annular jet from the air pumped out of the slot in the nozzle body. Note that the relatively low value of the axial velocity around $r = 0$ is compared to the jet inlet; this is caused by the shape of the induced flow streamtube, the divergent shape of the OCAJ nozzle, and the entrainment of the core flow into the annular injected jet.

Development of the OCAJ jet across a wider field of view was measured using PIV, see frame (a) of Fig. 10 showing the flow entering and leaving the nozzle and the flow to one side of the nozzle body revealing the inlet and exit details, refer to Fig. 6 for the sense of the field of view, axis system and flow directions. Figure 10(a) shows mean axial (u-) component magnitude with mean flow streamlines and flow direction superimposed. The annular jet can be seen as the region of high u velocity leaving the OCAJ body around $y/R = \pm 1$ with the lower u component closer to the body axis. The high momentum jets diffuse and eventually merge with increasing axial distance x. The flow speed around $y = 0$ initially decreases from the OCAJ exit plane but then begins to increase beyond $\frac{x}{R} \approx 1.5$. Similar behavior was reported by Padhani *et al.*[38] for their flow field survey of a similar jet system. Induced flow into the inlet side of the OCAJ is seen also, which is a result of the entrainment effect of the annular jet.

A. Comparison of the OCAJ and rotor wake baseline flow fields

For comparison, mean flow of the OCAJ and rotor are shown in Fig. 9 for LDA and Fig. 10 from PIV (frame (b) for the rotor wake). Figure 9 shows the large, low momentum zone $u/U_i \approx 0.25$ around 1 radius in diameter around the OCAJ axis, with rapid rise to peak jet velocity just further outboard before a fall to zero u outside the jet. The rotor flows show a distinct minimum momentum at the rotor axis,

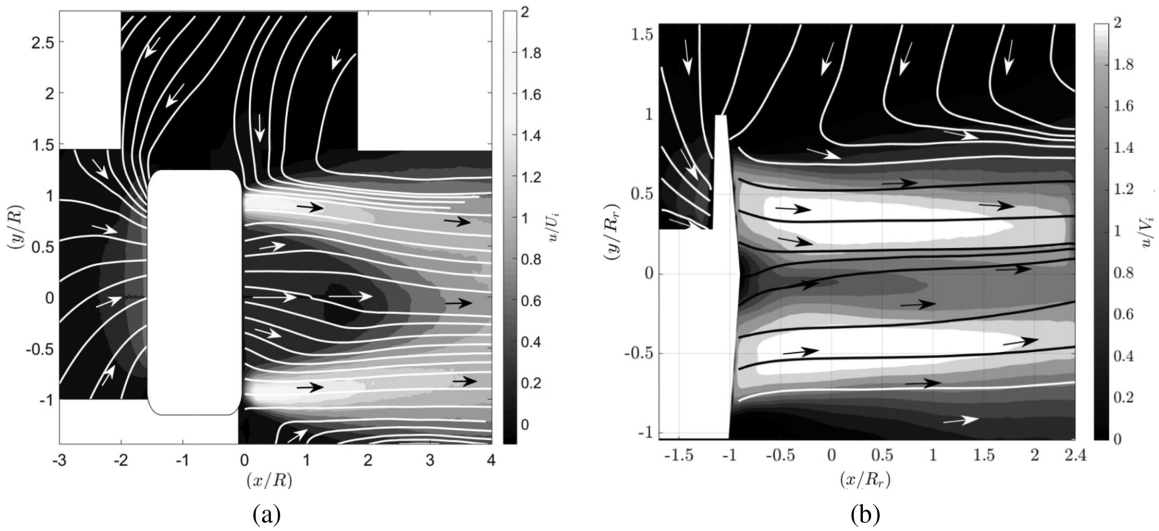

FIG. 10. Mean flow PIV of (a) OCAJ and (b) unshrouded rotor without shroud operating at $\alpha = 0$.

© Author(s) 2023

$u/V_i \approx 1.3$, rising rapidly further outboard with a more gentle fall to zero u outside the rotor wake. For the PIV measurement of the rotor in frame (b) of Fig. 10, lobes of higher momentum flow in the outboard regions are seen with lower momentum around the rotor axis. Note that the axis origin is selected as the exit plane of the rotor shroud when fitted, so the rotor disk plane in frame (b) is at $x/R_r = -1$. Axial velocity u increases along the axis from $\frac{x}{R_r} = 0$. Contrast this with the behavior for the OCAJ in frame (a) of Fig. 10 where there is an initial decrease in axial velocity then an increase beyond $\frac{x}{R} = 1.5$. In this respect, the OCAJ flow farther out from the OCAJ exit plane shows a stronger resemblance to the mean profiles of the rotor configuration.

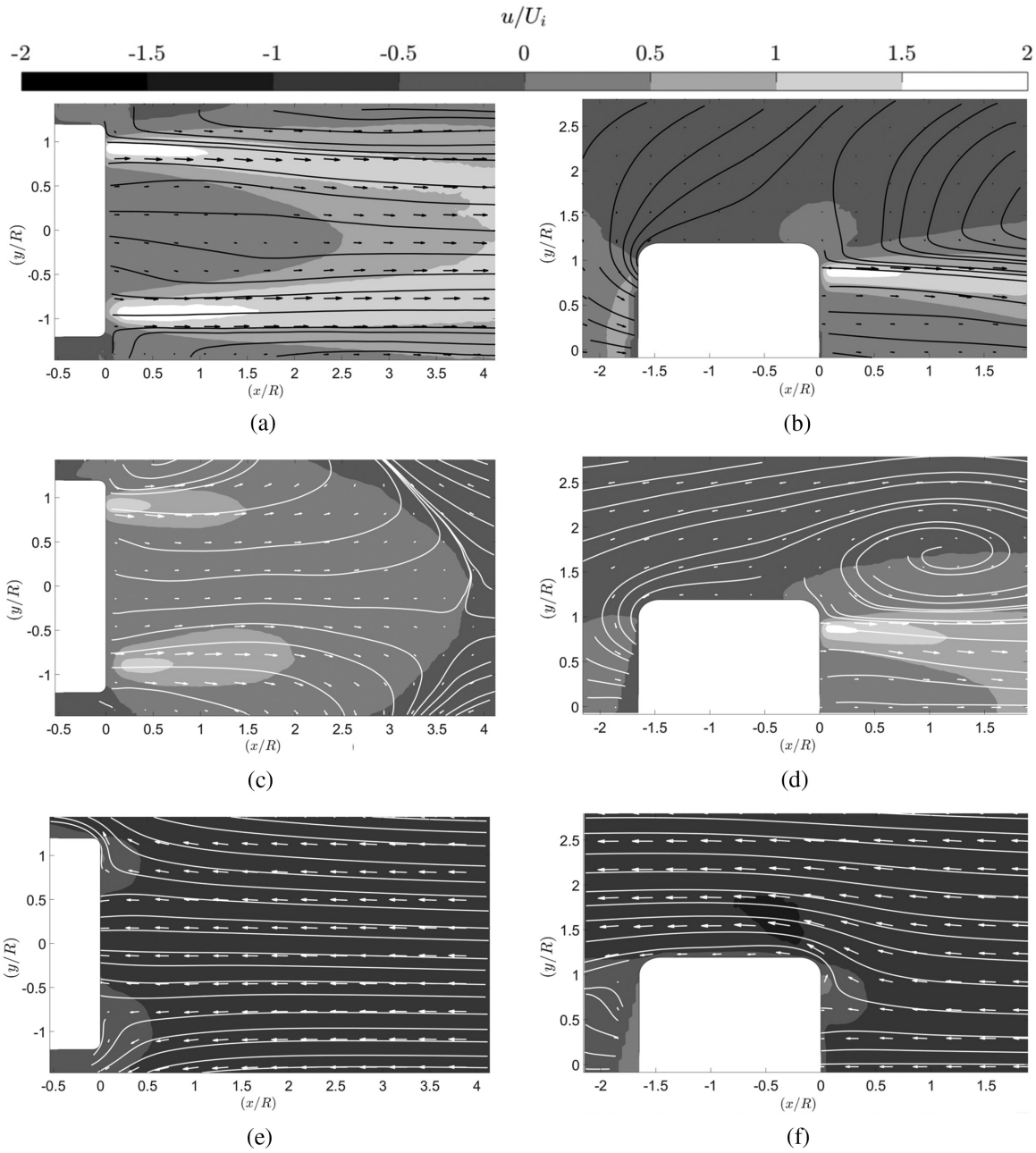

FIG. 11. Contour plots of averaged mean axial (u-) velocity of the ventilated OCAJ nozzle outlet (PIV regions 1 and 2) as counter flow ratio α increases. Wind tunnel flow is from right to left. Mean flow streamlines and a reduced number of velocity vectors are superimposed onto the contour plots. All of the velocity vectors are scaled with respect to the notional induced velocity U_i across OCAJ exit plane. The thick black line is zero counterflow, all other lines are at subsequently higher α. (a) $\alpha = 0.0$, region 1; (b) $\alpha = 0.0$, region 2; (c) $\alpha = 0.65$, region 1; (d) $\alpha = 0.65$, region 2; (e) $\alpha = 0.9$, region 1; and (f) $\alpha = 0.9$, region 2.

© Author(s) 2023

C. The OCAJ in counterflow

Tests were repeated with the wind tunnel running in counterflow to the OCAJ mean flow. The key parameter is α, the ratio of the counterflow velocity U_o to the OCAJ mean axial velocity in zero counterflow U_i. The flow field behavior with increasing counterflow velocity is revealed clearly using PIV. Figure 11 shows the development of the mean flow field upstream of the nozzle outlet and around the OCAJ body as the counter flow velocity was increased from $\alpha = 0.0$ to $\alpha = 0.9$. At low counterflow velocity ratios ($\alpha < 0.6$), not shown in this paper, the near flow field is similar to that of the ventilated OCAJ issuing into quiescent surroundings as shown in Fig. 10(a). As counterflow velocity increases at low α, the significant phenomenon in the mean flow velocity field is the movement of a saddle point from far away from the OCAJ exit plane toward the exit plane. Frames (a) and (b) of Fig. 11 show the two PIV regions at $\alpha = 0$ for subsequent comparison as α increases. Frame (c) shows the appearance of the saddle point feature in the field of view at $\alpha = 0.65$, where the saddle point is at $\frac{x}{R} \approx 3.5$. The saddle point is a topological feature on the mean flow streamline separating the counterflow from the OCAJ induced flow, and it moves toward the OCAJ exit plane rapidly for a small increase in counterflow velocity. Coincident with the appearance of the saddle point in frame (c), a large-scale mean flow recirculation appears, see frame (d) for PIV region 2 at $\alpha = 0.65$. Frames (e) and (f) at $\alpha = 0.9$ show the counterflow penetrating up to and through the OCAJ exit plane, with velocity vectors and mean flow streamlines at $\frac{y}{R} = \pm 1$ turning immediately out around the OCAJ body at the exit plane.

LDA measurements of the OCAJ flow in counterflow at the OCAJ exit plane are shown in Fig. 12. Increasing the counterflow velocity reduces the core flow u component, until the mean axial flow u around the axis $y = 0$ becomes negative (flow back into the nozzle), when significant v velocity magnitude (flow away from the axis) begins to develop close to $|y/R| = 1$. Further increase in counterflow velocity results in negative axial flow across the entire OCAJ exit plane, but the effects of the jet blowing are still evident in the u velocity profile.

The OCAJ flow in counterflow is highly unsteady, the mean flow features described above highlight the major changes in flow structure. The OCAJ flow around $\alpha = 0.6$–0.8 is characterized by expulsion events, where the wind tunnel counterflow penetrates right up to and into the OCAJ nozzle body from upstream, and a sudden flow reversal starting from within the OCAJ body develops, in which a powerful vortex system forms that envelops, sheds, and flows back around and through the OCAJ body and appears to push the counterflow back upstream. This is shown in a smoke flow visualization sequence in Fig. 13 at $\alpha = 0.7$, where the smoke wand is upstream in the wind tunnel relative to the OCAJ body. Frame (a)

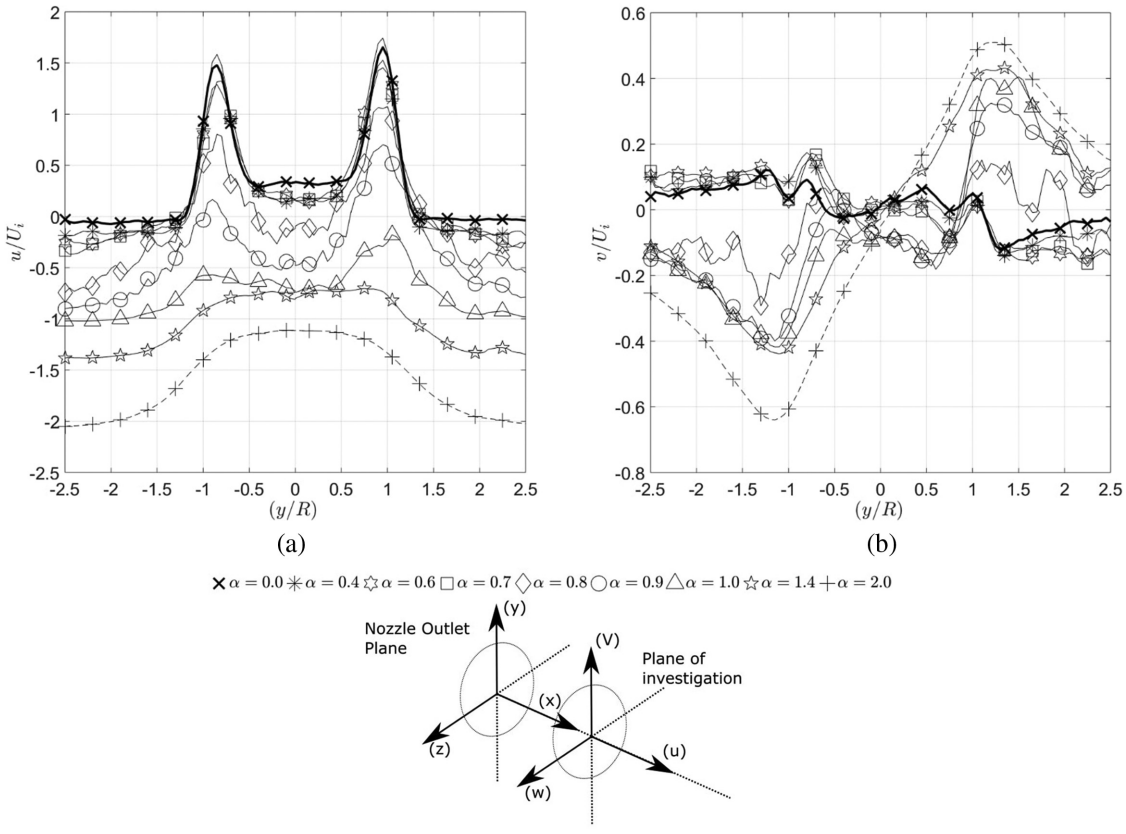

FIG. 12. Velocity profiles along the vertical axis of symmetry of the nozzle from LDA surveys of OCAJ in counterflow at the OCAJ exit plane. Frame (a) axial velocity component (u), frame (b) vertical velocity component (v). Data are scaled with respect to the notional induced velocity U_i at the OCAJ exit. The thick, black line is for zero counterflow.

© Author(s) 2023

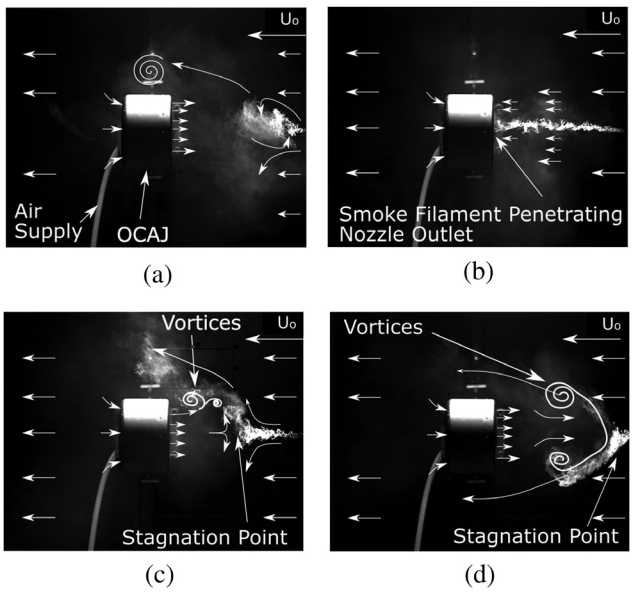

FIG. 13. Sequential smoke flow visualization images of an expulsion event observed when $\alpha = 0.7$ where $\beta = \frac{t|U_o|}{D}$, non-dimensional time scaled with counterflow velocity and OCAJ diameter. Wind tunnel counterflow is from right to left as indicated. Annotation indicates major features and flow directions from movie sequence. (a) $\beta = 0.0$; (b) $\beta = 5.7$; (c) expulsion event, $\beta = 8.19$; and (d) expulsion event, $\beta = 10.68$.

close to the end of an expulsion cycle shows the smoke filament just on the right hand side of the frame, and jet flow from left to right through the OCAJ body is indicated. Frame (b) shortly after shows the smoke filament penetrating right up to the nozzle exit plane, and the OCAJ is still inducing flow into its inlet side. An expulsion event takes place shortly after, and frame (c) shows the smoke filament from upstream has been pushed back upstream out of the OCAJ body. Swirling vortices are indicated in the smoke patterns, and a stagnation point observed in the flow is indicated. The stagnation point stays in the same general location for some time, and the smoke filament flaps up and down in response to the vortex patterns indicated. These move downstream and around the OCAJ body as indicated on frame (d). The mean position of the stagnation point is shown in the PIV as the saddle point, Fig. 11. Individual PIV images show significant variations from the mean flow picture as the flow field development proceeds, and Fig. 14 shows two such flow field states with frame (a) showing the counterflow penetrating the OCAJ exit plane and frame (b) with the OCAJ jet flow pushing out in the upstream direction during an expulsion event. Note the appearance of swirling, vortical patterns in the frame (b).

D. The rotor and shrouded rotor in descent (counterflow)

Figure 15 frames (a)–(f) show mean flow from PIV for the rotor and shrouded rotor at increasing descent rate α. The scaling velocity for the descent rate α for the rotor systems is $V_i = 3.34$ m/s, the mass flow averaged velocity measured at distance 1.48 rotor radii from the rotor disk plane $(x/R_r = 0.48)$. Frames (a) and (b) show zero counterflow for the two cases. Note that these are mean flow fields from measurements that are not phase averaged, and therefore, the instantaneous structure of the vortex wake is lost due to the averaging process; thus, for example, the unshrouded rotor helical vortex wake is not seen. Frames (c) and (d) at $\alpha = 1.0$ show the appearance of the saddle point in the field of view; it is at $\frac{x}{R_r} \approx 2$ for the rotor and at $\frac{x}{R_r} \approx 3$ for the shrouded rotor but note the offset of the rotor from the origin. Both these frames show the development of recirculation around the rotor system, but in the case of the shrouded rotor, frame (d), it is displaced somewhat outboard by the presence of the shroud body. As α increases the saddle point moves toward the rotor system, and frames (e) and (f) at $\alpha = 1.4$ show the counterflow has penetrated right up to the rotor plane and the shroud exit plane. The major observation is that the behavior of the shrouded rotor in descent is the same as the rotor; the shroud body has no significant effect on the development of the flow field, and a shrouded rotor wake collapses into a VRS in the same way as the isolated rotor.[41]

LDA surveys of the rotor flow with increasing counterflow at $x/R_r = -0.52$ are shown in Fig. 16. In zero counterflow, the width of the low-momentum zone close to the rotor axis is not so high, but there are two distinct peaks of high momentum flow. As counterflow speed increases the mean flow profile remains relatively unaffected

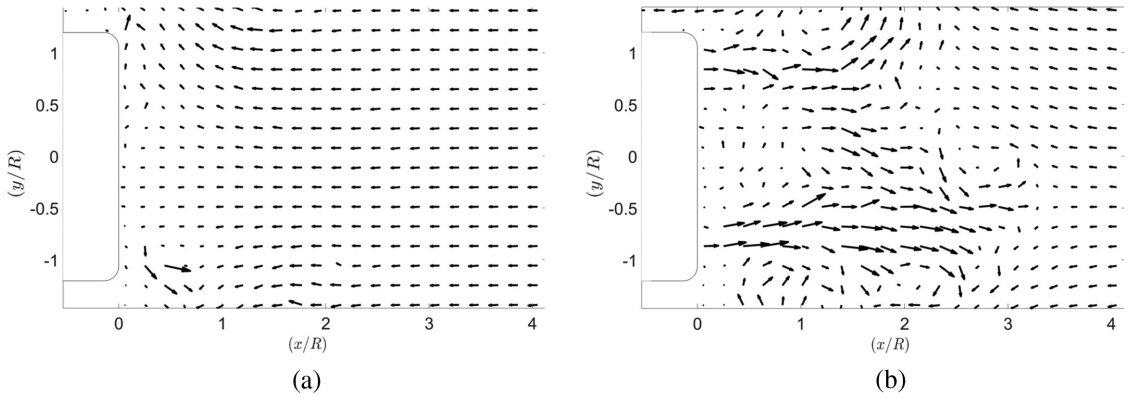

FIG. 14. Individual PIV snapshots during a VRS cycle of the OCAJ nozzle outlet (PIV: region 1) at $\alpha = 0.7$. These show the significant change of flow behavior observed during a VRS cycle. (a) flow into OCAJ body from upstream and (b) expulsion event with flow leaving OCAJ body.

© Author(s) 2023

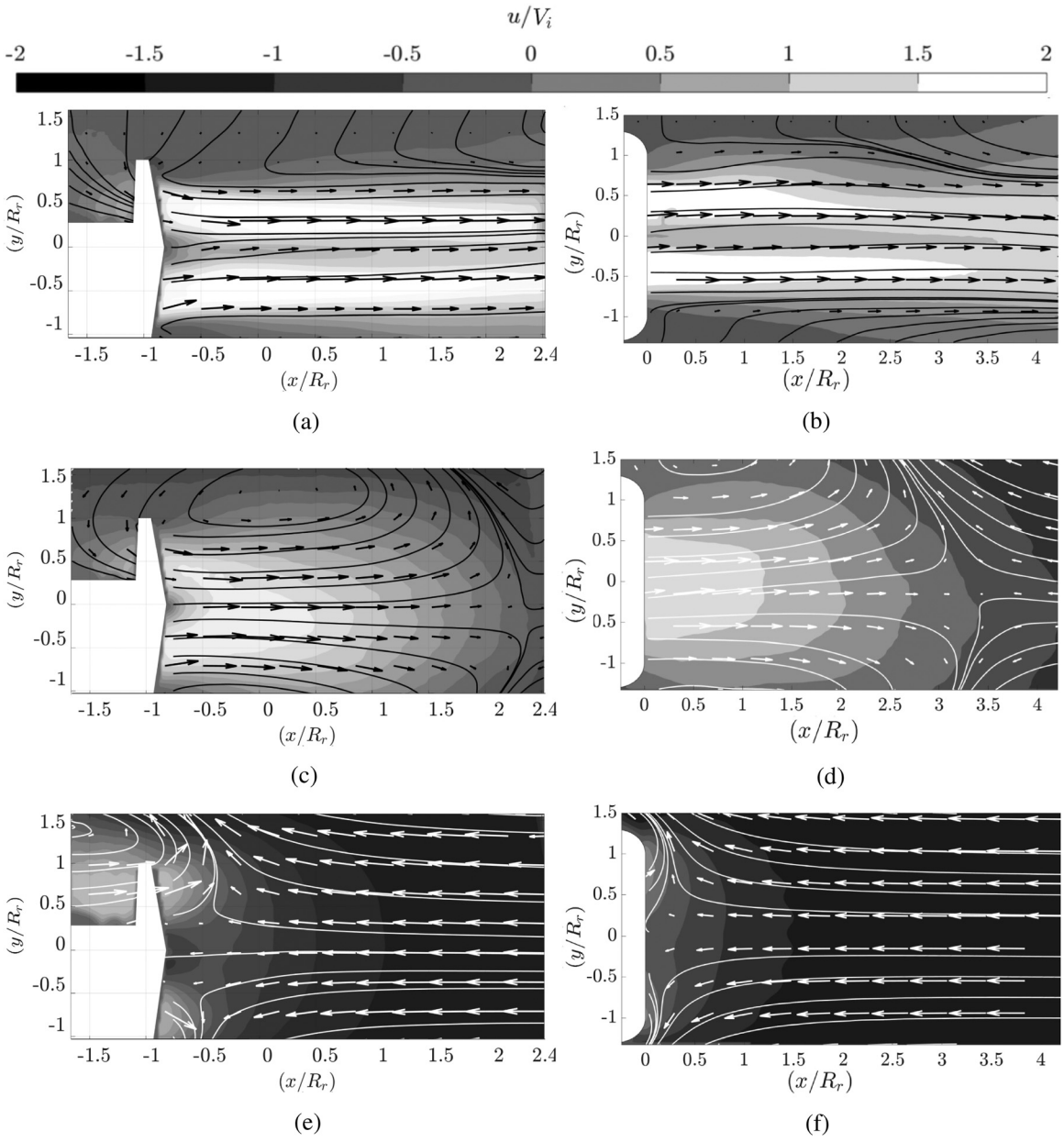

FIG. 15. Contour plots of averaged mean axial (u-) velocity of the rotor flow (PIV: region 1) as counter flow ratio α increases. Streamlines and a reduced number of velocity vectors are superimposed onto the contour plots. All of the velocity vectors are scaled with respect to the notional hover induced velocity V_i at a plane $(x/R_r = 1.48)$ from the rotor disk plane. (a) rotor at $\alpha = 0.0$, (b) shrouded rotor $\alpha = 0.0$, (c) rotor at $\alpha = 1.0$, (d) shrouded rotor at $\alpha = 1.0$, (e) rotor at $\alpha = 1.4$, and (f) shrouded rotor at $\alpha = 1.4$.

until the u component at $y = 0$ drops rapidly, which is accompanied by a fall in the u component magnitude in the outer peaks. This coincides with the appearance of high v magnitude flow away from the rotor axis. At sufficiently high α, a small zone of negative u is observed around $y = 0$ (a well-known feature of the VRS of a rotor), and eventually negative u is observed across the entire profile but the effort of the rotor acting against the counterflow is still evident.

IV. DISCUSSION

Features of the mean flow velocity field have been used to describe the changes to the flow field produced by a ventilated open core annular jet issuing into increasing counterflow. Results of a rotor and a shrouded rotor in experimentally simulated axial descent (counterflow) have been presented for comparison.

All three devices produce a similar mean flow structure in zero counterflow or descent as follows:

© Author(s) 2023

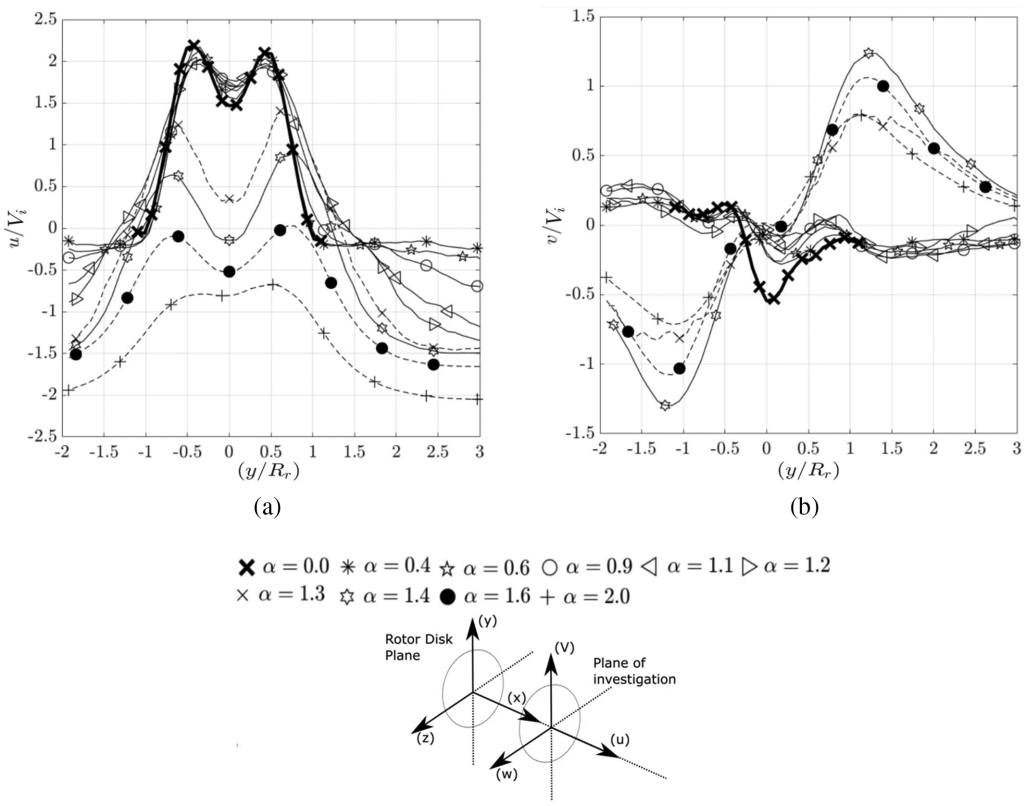

FIG. 16. Mean flow velocity profiles along the vertical axis of symmetry of the nozzle from LDA surveys of the rotor in counterflow ($x/R_r = -0.52$). Frame (a) axial velocity component (u), frame (b) vertical velocity component (v). Data are scaled with respect to the notional hover induced velocity V_i at a plane $x/R_r = 1.48$ from the rotor disk plane. The thick black line is for zero counterflow.

- Flow leaving the OCAJ nozzle body has a ring of high momentum flow surrounding a lower momentum core flow.
- Flow leaving the rotor or the shrouded rotor body has high momentum in the rotor tip region, and lower momentum around the rotor axis.
- Flow is drawn into the OCAJ body inlet by entrainment effect due to the annular jet.
- Flow is induced into the rotor disk or shrouded rotor body inlet by the action of the rotor rotation (aerodynamic lift).

The major difference between the OCAJ and the rotor flows is the manner in which momentum in introduced to the flow. In the OCAJ, it is by injection of mass flow containing momentum through the annular slot running around the inward facing surface of the OCAJ. In the case of the rotor systems it is by the action of blade section aerodynamic lift due to rotor rotation and blade section aerodynamic performance. The unshrouded rotor subsequently trails a helical vortex wake (root and tip vortices from each blade), while in the case of the shrouded rotor, the formation of the tip vortices is disrupted due to the close spacing between the shroud surface and the blade tips. Mean flow images of the unshrouded and shrouded rotors and the OCAJ in zero descent rate or counterflow are shown in frames (a) and (b) of Figs. 11 and 15, but Fig. 17 shows a sample instantaneous vorticity plot for each of these flows. Frame (a) of this figure for the rotor shows a cross section of the trailed helical vortex wake, and the rotor blade tip and root vortices can be seen. These features are highly attenuated for the shrouded rotor, frame (b). The OCAJ case, frame (c) of Fig. 17, shows a cross section of the instantaneous jet shear layer. Note that the OCAJ jet vorticity is very low, and it has been plotted on a different scale compared to the rotor cases. There is rapid, turbulent diffusion of the jet after it leaves the OCAJ body, and the wide irrotational core of the jet at the exit plane of the jet body at $x/R = 0$ helps to reveal the extent of rapid jet diffusion as the shear layers meet.

The collapse of a rotor wake into VRS is well-known, and the phenomenon has been described for a wide range of Reynolds numbers and rotor blade parameters; it is a feature of the rotor wake behavior. The features of this collapse are: the appearance of the saddle point close to the rotor disk; reversed flow penetrating up to the rotor disk, the development of a toroidal flow topology; and highly unsteady flow, with repeated formation and shedding of the vortex ring. The rotor blade tip and root trailed vortices mingle and interact during the VRS process. With the shrouded rotor these trailed vortex features are somewhat attenuated,[41] but there is a VRS formation that is strikingly similar to the isolated rotor. The development of the OCAJ in counterflow demonstrates the same features, with the incursion of the counterflow and appearance of the saddle point close to the exit plane, and the same observations of the highly unsteady flow with the formation

© Author(s) 2023

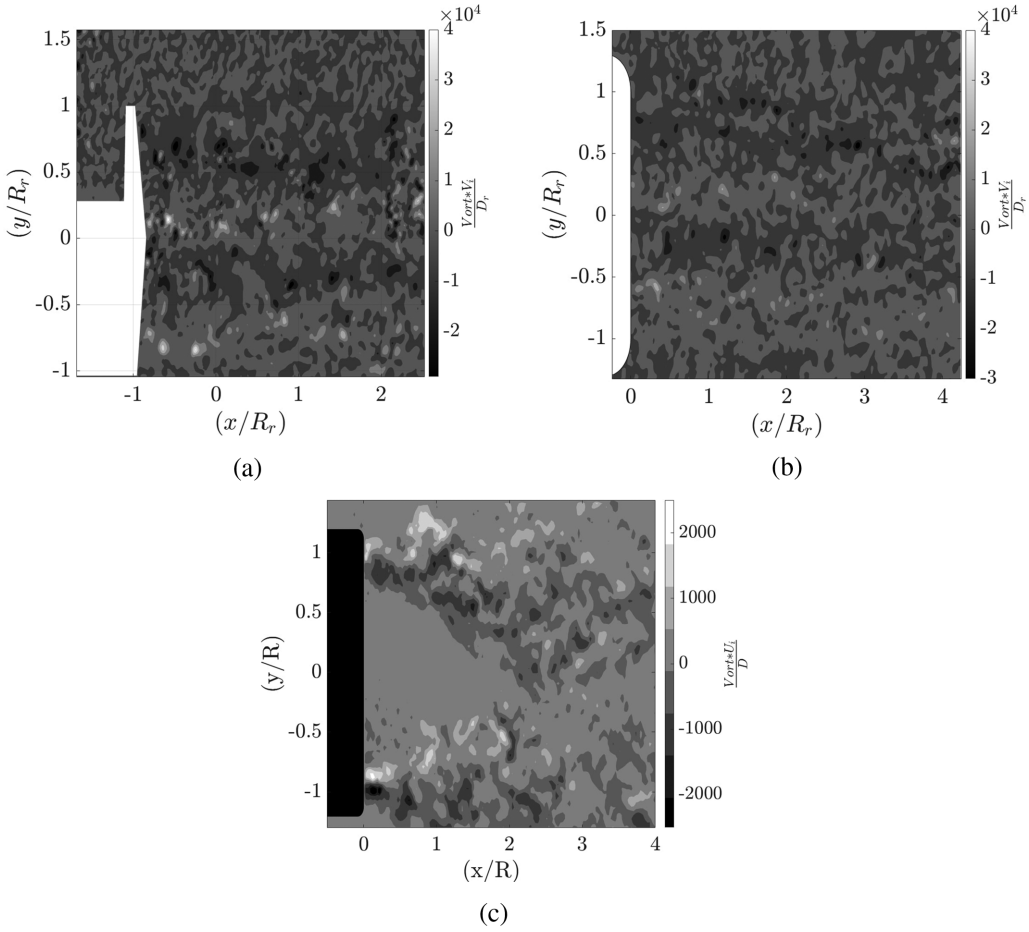

FIG. 17. Instantaneous vorticity plots of the flow field produced by the unshrouded rotor (a), the shrouded rotor (b) and the OCAJ (c) at $\alpha = 0$. The vorticity levels are scaled with their respective induced velocity (U_i, V_i) and diameters (D, D_r).

of a vortex ring that breaks down, sheds, and reforms. For the OCAJ, the jet breakdown in counterflow is accompanied by the appearance of strong vorticity clumps, such features are evident in Fig. 14 frame (b), but these are not the highly connected helical vortices of the rotor. The rotor mean flow and the OCAJ jet mean flow in zero counterflow both contain neighboring regions of oppositely signed vorticity, but the OCAJ jet does not contain the distinctive trailing vortices of a rotor. The rotor wake, on the other hand, is in fact a jet flow, and it is perhaps better to regard the rotor wake as a jet flow with a trailing vortex wake embedded in it for the purposes of comparison of the two VRS flows described in this paper. Descriptions of vortex pairing mechanisms in the observed development of the rotor VRS may then be observations of smaller scale, but significant, fluid dynamic events, rather than phenomena driving the large scale VRS.

The OCAJ flow first shows evidence of collapse into its VRS at a much lower counterflow velocity that the equivalent descent rate for the rotor. As shown above in Fig. 9, the OCAJ exit flow has a wide region of almost uniform, low momentum flow centered on the body axis, while the rotor wake shows a sharp dip to the minimum momentum along the rotor axis, and the zone of low momentum is very small. A rotor blade is designed to generate thrust along its span, so a wide region of low momentum flow across a rotor wake would signify a poor blade design. This could be the result of using a large spanwise extent of a non-lifting surface starting from the blade root. A rotor like this with a large root cutout was tested as part of the series of tests conducted as part of the wider study behind this paper,[47] and this formed a VRS in a similar manner to any rotor flow but at lower descent velocity ratio α between 0.6 and 0.7. Since the primary objective of the current study was to generate mean flow fields with similar topologies, neither a parametric study of the OCAJ mass flow rate and nozzle features nor a parametric study of rotor characteristics and shroud shape was performed.

We propose that the process of the formation of the vortex ring state in the context of this paper is that of a breakdown of a particular jet flow profile due to its interaction with a counterflow. The counterflow can penetrate the center of the jet relatively easily due to the lower momentum flow close to the jet axis. As a result, the higher momentum outer portions of the jet are displaced from one another and deflected outwards. The behavior of round jets in counterflow has been studied extensively, for example, by Yoda and Fiedler.[34] Here, the

© Author(s) 2023

jet tip can oscillate regularly, or appear to show larger amplitude excursions of penetration extent dependent on the jet-to-counterflow velocity ratio, and there is particular sensitivity to the inclination angle of the jet. For the OCAJ jet in this paper, deflection of the high momentum outer part of the jet by the penetration of the counterflow into the low momentum core would lead to a subsequent change of inclination angle of that region of the jet, driving its dynamics in a different way.

V. CONCLUSIONS

Experiments on the fluid dynamics of a rotor descent into its own wake and an open core-annular jet in counterflow have been described and comparisons made between the two. The mean flow features of the jet flow in zero counterflow resemble those of the rotor wake mean flow in hover, but the jet flow forms a continuous, axisymmetric shear layer that does not contain the highly connected, helical vortex structure of the rotor wake. As the counterflow velocity relative to the jet flow is increased, the jet mean flow develops in a manner similar to the flow of the rotor wake in axial descent, until at sufficiently high counterflow speed a flow state that resembles the vortex ring state of a rotor is observed. The important topological features shared by these two flows in their respective vortex rings states are: a penetration of reversed flow along the jet or rotor axis up to the jet body or rotor disk; a stagnation or saddle point; a toroidal vortex of the same order of size as the whole jet body or rotor that sheds and reforms; and a highly unsteady, transient behavior that switches between a flow resembling the normally observed form of the jet or rotor wake and one dominated by the reverse flow penetrating right up to the jet orifice or rotor disk. We propose that a theoretical and experimental treatment of the behavior of the particular jet flow velocity profile in a counterflow could lead to enhanced understanding of the dynamics of the vortex ring state of a rotor.

ACKNOWLEDGMENTS

The experiments were conducted using instrumentation provided by UK National Wind Tunnel Facility supported by the UK EPSRC, Grant No. EP/L024888/1.

AUTHOR DECLARATIONS

Conflict of Interest

The authors have no conflicts to disclose.

Author Contributions

David J. Pickles: Conceptualization (equal); Data curation (equal); Formal analysis (equal); Investigation (equal); Methodology (equal); Validation (equal); Visualization (equal); Writing – original draft (equal); Writing – review & editing (equal). **Richard Green:** Conceptualization (equal); Data curation (supporting); Formal analysis (supporting); Funding acquisition (lead); Investigation (equal); Methodology (equal); Project administration (equal); Resources (equal); Software (equal); Supervision (equal); Validation (equal); Writing – original draft (equal); Writing – review & editing (equal). **Angela Busse:** Formal analysis (equal); Supervision (equal); Writing – original draft (equal); Writing – review & editing (equal).

DATA AVAILABILITY

The data that support the findings of this study are available from the corresponding author upon reasonable request.

REFERENCES

[1]P. Martin, M. Bhagwat, and J. Leishman, "Visualization of a helicopter rotor wake in hover," in 17th AIAA Applied Aerodynamics Conference, 1999.
[2]G. De Bothezat, "The general theory of blade screws," NACA Report No. 29 (NACA, 1919).
[3]J. P. Reeder and F. B. Gustafson, "On the flying qualities of helicopters," Report No. NACA-TN-D-1799 (NACA, 1949).
[4]P. Brotherhood, "Flow through a helicopter rotor in vertical descent," Report No. 2735 (Aeronautical Research Committee, 1949).
[5]W. Stewart, "Helicopter behaviour in the vortex-ring conditions," Report No. 3117 (Aeronautical Research Council, 1951).
[6]J. M. Drees and W. P. Hendal, "Airflow patterns in the neighbourhood of helicopter rotors," J. Aircr. Eng. **23**, 107–111 (1951).
[7]W. R. M. V. Hoydonck, H. Haverdings, and M. D. Pavel, "A review of rotorcraft wake modelling methods for flight dynamics applications," in 35th European Rotorcraft Forum, Hamburg, 2009.
[8]J. R. Dailey, N. R. Augustine, J. B. Davis, and E. E. Covert, "Report of the panel to review the V-22 program" (Memorandum Secretary Defence, 2001).
[9]V. Leble and G. Barakos, "Forced pitch motion of wind turbines," J. Phys.: Conf. Ser. **753**, 022042 (2016).
[10]R. Kyle, Y. C. Lee, and W. Früh, "Propeller and vortex ring state for floating offshore wind turbines during surge," J. Renewable Energy **155**, 645–657 (2020).
[11]A. Gessow, "Flight investigation of effects of rotor blade twist on helicopter performance in the high-speed and vertical-autorotation-descent conditions," NACA TN No. 1666 (NACA, 1948).
[12]C. N. Lock, H. Bateman, and H. C. H. Townsend, "An extension of the vortex theory of airscrews with applications to airscrews of small pitch, including experimental results," Report No. 1014 (Aeronautical Research Council, 1925).
[13]H. Glauert, "The analysis of experimental results in the windmill brake and vortex ring states of an airscrew," Report No. 1026 (Aeronautical Research Council, 1926).
[14]W. Castles and R. B. Gray, "Empirical relationship between induced velocity, thrust, and rate of descent of a helicopter rotor as determined by wind tunnel tests on four model rotors," NACA TN No. 2474 (NACA, 1951).
[15]S. Newman, R. E. Brown, J. Perry, S. Lewis, M. Orchard, and A. Modha, "Predicting the onset of wake breakdown for rotors in descending flight," J. Am. Helicopter Soc. **48**, 28–38 (2003).
[16]P. Spalart, "On the simple actuator disk," J. Fluid Mech. **494**, 399–405 (2003).
[17]A. Taghizad, L. Binet, J. Jimenez, and D. Heuze, "Experimental and theoretical investigations to develop a model of rotor aerodynamics adapted to steep descents," in *58th Annual Forum* (American Helicopter Society, Montreal, 2002).
[18]P. F. Yaggy and K. W. Mort, "Wind-tunnel tests of two VTOL propellers in descent," Report No. NASA TN D-1766 (NASA Ames Research Center, 1962).
[19]K. Washizu, A. Azuma, J. Koo, and T. Oka, "Experiments on a model helicopter rotor operating in the vortex ring state," J. Aircraft. **3**, 225–230 (1966).
[20]A. Azuma and A. Obata, "Induced flow variation of the helicopter rotor operating in the vortex ring state," J. Aircraft **5**, 381–386 (1968).
[21]S. Newman, R. Brown, F. Perry, G. Ahlin, I. Simmons, "A. Modha, and M. Khelifa, Revisiting the effects of blade geometry on rotor behaviour in descending flight," in 30th European Rotorcraft Forum, Marseilles, France, 2004.
[22]P. Brinson, "Experimental investigation of the vortex ring condition," in 24th European Rotorcraft Forum, Marseille, 1998.
[23]S. Chae, S. Lee, and J. Kim, "Effects of rotor-rotor interaction on the wake characteristics of twin rotors in axial descent," J. Fluid Mech. **952**, A31 (2022).
[24]J. Stack, F. X. Caradonna, and Ö. Savaş, "Flow visualizations and extended thrust time histories of rotor vortex wakes in descent," J. Am. Helicopter Soc. **50**, 279–288 (2005).
[25]Ö. Savaş, R. B. Green, and F. X. Caradonna, "Coupled thrust and vorticity dynamics during vortex ring state," J. Am. Helicopter Soc. **54**, 22001 (2009).

© Author(s) 2023

[26]R. B. Green, E. A. Gillies, and R. E. Brown, "The flow field around a rotor in axial descent," J. Fluid Mech. **534**, 237–261 (2005).
[27]G. J. Leishman, M. J. Bhagwat, and S. Ananthan, "The vortex ring state as a spatially and temporally developing wake instability," J. Am. Helicopter Soc. **49**, 160–175 (2004).
[28]J. M. Bhagwat and G. J. Leishman, "Stability analysis of helicopter rotor wakes in axial flight," J. Am. Helicopter Soc. **45**, 165–178 (2000).
[29]S. Ananthan and J. G. Leishman, "Rotor wake aerodynamics in large amplitude maneuvering flight," J. Am. Helicopter Soc. **51**, 225–243 (2006).
[30]R. E. Brown, "Rotor wake modelling for flight dynamic simulation of helicopters," AIAA J. **38**, 57–63 (2000).
[31]A. G. Ahlin and R. E. Brown, "Wake structure kinematics in the vortex ring state," J. Am. Helicopter Soc. **54**, 32003 (2009).
[32]O. König and H. E. Fiedler, "The structure of round turbulent jets in counterflow: A flow visualization study," in *Advances in Turbulence III*, edited by A. V. Johansson and P. H. Alfredsson (Springer, Berlin, 1991), pp. 61–66.
[33]D. F. Hopkins and J. M. Robertson, "Two-dimensional incompressible fluid jet penetration," J. Fluid Mech. **29**, 273–287 (1967).
[34]M. Yoda and H. E. Fiedler, "The round jet in a uniform counterflow: Flow visualization and mean concentration measurements," J. Exp. Fluids **21**, 427–436 (1996).
[35]P. D. Gammack, F. Nicolas, and K. J. Simmonds, "Bladeless fan," US Patent No. 8,308,445 B2 (2008).
[36]M. Jafari, H. Afshin, B. Farhanieh, and H. Bozorgasareh, "Numerical aerodynamic evaluation and noise investigation of a bladeless fan," J. Appl. Fluid Mech. **8**, 133–142 (2015).
[37]M. Jafari, A. Sojoudi, and P. Hafezisefat, "Numerical study of aeroacoustic sound on performance of bladeless fan," Chin. J. Mech. Eng. **30**, 483–494 (2017).
[38]S. A. Padhani, G. R. Hunt, and T. N. Jukes, "The turbulent jet from a slender annular slot ventilated by a self induced flow through the open core," J. Phys Rev. Fluids **3**, 014602 (2018).
[39]H. Coandă, Lifting device coanda effect (1936). US Patent.
[40]J. L. Pereira, "Hover and wind-tunnel testing of shrouded rotors for improved micro air vehicle design," Ph.D. thesis (DRUM University of Maryland Libraries, 2008).
[41]D. Pickles, D. Zagaglia, A. Busse, and R. Green, "Vortex ring state of a shrouded rotor: An experimental survey," Exp. Fluids **64**, 69 (2023).
[42]PIVTechGmbH, see https://www.pivtec.com/ for "Pivpart160 Product Information (2019)" (last accessed April 14, 2019).
[43]W. K. George, "Quantitative measurement with the burst-mode laser Doppler anemometer," J. Exp. Therm. Fluid Sci. **1**, 29–40 (1988).
[44]H. E. Albrecht, M. Borys, N. Damaschke, and C. Tropea, *Laser Doppler and Phase Doppler Measurement Techniques* (Springer Science and Business Media, 2003).
[45]L. Gui and S. T. Wereley, "A correlation-based continuous window-shift technique to reduce the peak-locking effect in digital PIV image evaluation," Exp. Fluids **32**, 506–517 (2002).
[46]W. D. Morgan, B. J. Brinkworth, and G. V. Evans, "Upstream penetration of an enclosed counterflowing jet," Ind. Eng. Chem. Fundam. **15**, 125–127 (1976).
[47]D. J. Pickles, "A series of experimental investigations into different manifestations of the vortex ring state," Ph.D. thesis (University of Glasgow, Scotland, UK, 2020).

© Author(s) 2023